

Selective C–C Coupling by Spatially Confined Dimeric Metal Centers

Yanyan Zhao, Si Zhou^{*}, Jijun Zhao

SUMMARY

Direct conversion of carbon dioxide (CO₂) to high-energy fuels and high-value chemicals is a fascinating sustainable strategy. For most of the current electrocatalysts for CO₂ reduction, however, multi-carbon products are inhibited by large overpotentials and low selectivity. For practical applications, there remains a big gap of knowledge in proper manipulation of the C–C coupling process. Herein, we exploit dispersed 3*d* transition metal dimers as spatially confined dual reaction centers for selective reduction of CO₂ to liquid fuels. Various nitrogenated holey carbon monolayers are shown to be promising templates to stabilize these metal dimers and dictate their electronic structures, allowing precise control of the catalytic activity and product selectivity. By comprehensive first-principles calculations, we screen the suitable transition metal dimers that universally have high activity for ethanol (C₂H₅OH). Furthermore, remarkable selectivity for C₂H₅OH against other C₁ and C₂ products is found for Fe₂ dimer anchored on C₂N monolayer. The correlation between the activity and *d* band center of the supported metal dimer as well as the role of electronic coupling between the metal dimer and the carbon substrates are thoroughly elucidated.

Keywords: metal dimer, holey carbon monolayer, CO₂ conversion, C₂ products, selectivity

Key Laboratory of Materials Modification by Laser, Ion and Electron Beams (Dalian University of Technology),
Ministry of Education, Dalian 116024, China

^{*} Correspondence: sizhou@dlut.edu.cn (Si Zhou)

INTRODUCTION

Production of liquid fuels by catalytic conversion of CO₂, the main greenhouse gas and meanwhile an abundant carbon feedstock, has been regarded as an appealing strategy to solve both energy and environmental crises, albeit facing great challenges (Birdja et al., 2019; Jia et al., 2019; Amal et al., 2017). Copper-based materials have been widely adopted as catalysts for electro-reduction of CO₂ to multi-carbon (C₂ or C₂₊) products (Zheng et al., 2019). Although fairly good activity can be achieved by modification or morphology engineering of copper, such as sculpturing it into nanoparticles or nanocubes, doping or alloying, and making oxide-derived copper, the selectivity and efficiency of most copper-based electrocatalysts remain unsatisfactory for commercialization of the CO₂ conversion technique to high-energy fuels and high-value chemicals (Kim et al., 2017; Zhou et al., 2018; Gao et al., 2019; Wang et al., 2018).

Recently, transition metal atoms dispersed on nitrogen-doped porous carbon nanomaterials emerge as a promising category of electrocatalysts for CO₂ reduction, which have maximum atomic efficiency, high electrical conductivity and good durability, and can be facilely synthesized in the laboratory (Wang et al., 2019; Bayatsarmadi et al., 2017; Chen et al., 2019; Cheng et al., 2018). The transition metal atoms are usually anchored in the pores of the carbon matrix and coordinated with the nitrogen atoms, exhibiting unique electronic states and acting as isolated reaction centers for CO₂ reduction. Remarkable activity and selectivity toward carbon monoxide (CO) has been observed for various dispersed transition metal atoms (Fe, Co, Ni, Mn, and Cu) on N-doped graphene, carbon nanosheets or nanospheres, with selectivity up to 97% and Faradaic efficiency above 80% (Jiang et al., 2018; Zhang et al., 2018; Yang et al., 2018; Wang et al., 2019; Ren and Zhao, 2019). First-principles calculations show that the activity highly depends on the type of metal atoms, which provide different binding strengths with the reaction intermediates (Ju et al., 2017). The single metal sites also have an advantage of suppressing the competing hydrogen evolution reaction (HER), due to the unique adsorption configuration of H* species compared to those on

the transition metal surfaces (Bagger et al., 2017).

Furthermore, homonuclear and heteronuclear dimers of transition metal immobilized in carbon based nanostructures, such as Fe₂ and Fe-Co on nitrogenated graphitic carbon materials, Fe-Ni on N-doped graphene, and Pt-Ru on g-C₃N₄, have been synthesized in the laboratory (Ye et al., 2019; Wang et al., 2017; Wang et al., 2018; Zhou et al., 2019). This opens up the windows for a broader range of chemical processes that require dual reaction centers either with enhanced activity or carrying different functionalities simultaneously. For instance, Ren et al. fabricated diatomic Fe-Ni sites embedded in nitrogenated carbon (Ren et al., 2019). By taking advantage of the strong binding capability of Fe with CO₂ molecule and the weak adsorption of CO on Ni, they achieved impressively high selectivity of 99% for CO and Faradaic efficiency above 90% over a wide potential range from -0.5 to -0.9 V, reaching 98% at -0.7 V vs. reversible hydrogen electrode (RHE). On the theoretical side, a Cu₂ dimer supported on the C₂N monolayer was predicted to have high selectivity for methane (CH₄), while dimerization of two CO species leading to the formation of ethene (C₂H₄) is possible with an energy cost of 0.76 eV (Zhao et al., 2018). Other C₁ products have also been proposed for elementary and mixed metal dimers on various N-coordinated carbon nanostructures, including defective graphene and phthalocyanine (Li et al., 2015; He et al., 2018; Shen et al., 2017).

Intuitively, two adjacent metal atoms that are spatially confined in a hole of N-doped carbon materials can provide unique active sites, which not only enable the simultaneous fixation of two CO₂ molecules, but also sterically limit the reaction pathways that may be beneficial for C-C coupling toward C₂ or C₂₊ products. Moreover, various combinations of metal dimers and carbon substrates give high degrees of freedom for modulating the catalytic performance. However, the atomistic mechanism and composition recipe of such heterogeneous catalysts remain largely unknown, which impede their rational design and experimental synthesis for practical uses.

Here we exploit 3*d* transition metal dimers immobilized on various nitrogenated holey carbon sheets for selective reduction of CO₂ to C₂ products. By systematic first-

principles calculations, the detailed C–C coupling mechanism on the spatially confined dual metal centers has been elucidated for the first time. The suitable transition metal elements and carbon substrates that lead to high activity and selectivity for ethanol (C_2H_5OH) and C_2H_4 are screened, and the underlying electronic structure-activity relationship is unveiled. These theoretical explorations illuminate important clues for precisely engineering the dispersed metal catalysts on porous carbon nanomaterials for direct conversion of greenhouse gas to multi-carbon hydrocarbons and oxygenates.

RESULTS and DISCUSSION

In the laboratory, N-doped graphitic carbon materials with controllable doping contents (up to 16.7% of N content) and atomic geometries can be achieved via either direct synthesis or post treatment (Xue et al., 2012; Xu et al., 2018; Qu et al., 2010). Here we focused on pyridine N dopants in graphene, which are the main doping species at high N contents and are usually associated with the vacancies or pores of the carbon basal plane (Sheng et al., 2011; Sarau et al., 2017). As displayed in Figure 1, we considered a series of N-doped holey graphene monolayers, comprising C vacancies of various sizes (denoted as V_n , $n = 2, 3, 4, 6$) with the edges coordinated with different numbers of N atoms (denoted as mN , $m = 4, 5, 6$). Specifically, 4N- V_2 , 5N- V_3 and 6N- V_4 systems can be viewed as four, five and six N atoms decorating the edges of di-vacancy, tri-vacancy and tetra-vacancy in graphene, respectively, all of which have been commonly observed in experiment (Lin et al., 2015; He et al., 2014; Wang et al., 2018). Note that, the V_6 pore in graphene is a favorable defect according to transmission electron microscopy experiment (Robertson et al., 2015), and our previous calculation showed that N-doped V_6 (namely 6N- V_6) has extraordinary thermodynamic stability (Luo et al., 2013). Besides the N-doped graphitic sheets, we also considered the synthetic carbon nitride monolayers, including g- C_3N_4 and C_2N (Zhao et al., 2014; Mahmood et al., 2015). All these porous N-coordinated carbon sheets have formation energies (defined by Equation S1 in Supplemental Information) in the range of 0.16 ~ 0.21 eV/Å, while the N-free V_6 is higher in energy by over 0.46 eV/Å than the others

(Table 1). These nitrogenated 2D holey carbon materials are ideal templates to stabilize and disperse metal atoms or small clusters. Indeed, isolated Fe₂, Fe-Ni, and Fe-Co dimers embedded in 6N-V₄(a), as well as Fe₂ and Pt-Ru dimers anchored on g-C₃N₄ have already been realized in experiment (Ye et al., 2019; Wang et al., 2017; Zhou et al., 2019; Ren et al., 2019; Tian et al., 2018).

To evaluate the capability of various supported metal dimers for CO₂ reduction toward C₂ products, we first explored the atomic structures, electronic and adsorption properties of dimeric 3d transition metal clusters on the 6N-V₆ monolayer (as will be shown later, this substrate gives metal dimers the highest activity for CO₂ reduction). As presented in Figure 1 and Figure S1, all metal dimers are embedded in the hole of the graphitic sheet, except that Sc₂ with a larger atomic size induces a noticeable buckling of 0.94 Å in the out-of-plane direction. Four N–metal bonds are formed with bond length of 1.95 ~ 2.09 Å, and the metal–metal bond length ranges from 1.96 Å to 2.79 Å (Table 2). The binding energy (defined by Equation S2 in Supplemental Information) between the metal dimer and the graphitic sheet is –4.29 ~ –10.28 eV, excluding the possibility of dissociation or aggregation of the metal dimer. The thermal stability of these carbon substrate anchored metal dimers was further assessed by *ab initio* molecular dynamics (AIMD) simulations, which manifest that they can sustain at least 800 K for 10 ps with small vertical displacement of metal atoms (< 0.2 Å) (see Figure S2 for details), suggesting superior thermal stability for practical uses.

A CO₂ molecule can favorably chemisorb on these dispersed metal dimers except Cu₂. The molecule is bended in the bidentate configuration with O–C–O angle of 124.90 ~ 141.96°. The C atom and one of the O atoms of CO₂ form two bonds with the underlying metal atoms; the C–O bond length is elongated to 1.21 ~ 1.36 Å, compared to 1.16 Å for a free CO₂ molecule. The adsorption energy (defined by Equation S3 in Supplemental Information) of CO₂ ranges from –0.82 eV to –3.40 eV. Overall speaking, stronger binding is provided by the metal element with fewer *d* electrons. The trend of activity can be understood by the electronic density of states (DOS) shown in Figure 2a. Taking Fe₂@6N-V₆ as an example, hybridization between the *d* orbitals of Fe₂ dimer

and the p orbitals of 6N-V₆ monolayer substrate is evident, with prominent electronic states at the vicinity of the Fermi level mainly contributed by the Fe atoms. Electron transfer of 0.73 e occurs from Fe₂ to 6N-V₆ monolayer, which lifts the Fermi level of the hybrid system above the $2\pi^*$ state of CO₂. As a result, Fe₂@6N-V₆ can favorably donate about 0.71 electrons to the antibonding orbital of CO₂, as manifested by the differential charge densities in Figure 3a. As depicted in Figure 2b, CO₂ adsorption energy generally follows a linear relationship with the d band center of the supported metal dimers (relative to the Fermi level), as the metal dimer with a higher d band center would provide stronger binding with CO₂ (Hammer et al., 2000).

In addition, we examined the capability of various dispersed 3d transition metal dimers for activating two CO₂ molecules simultaneously, which is a prerequisite for C–C coupling to yield C₂ products. Several candidate systems including Sc₂, Ti₂, Cr₂, Mn₂ and Fe₂ dimers on the 6N-V₆ monolayer have adsorption energies of $-3.71 \sim -0.48$ eV for fixation of two CO₂ molecules (Figure 3 and Figure S3), while the other metal dimers are only able to bind one CO₂ molecule. Considering that Fe is an earth-abundant element and dispersed Fe atoms and dimers can be readily obtained in the experiment (Ye et al., 2019; Tian et al., 2018), thereafter we explored Fe₂ dimer on various nitrogenated 2D holey carbon materials as a representative of dual metal centers.

Figure 1 presents the structures of a Fe₂ dimer immobilized on several 2D carbon substrates. The dimer forms 4 ~ 6 bonds with the neighboring N or C atoms, having bond lengths of 1.91 ~ 2.21 Å for Fe–Fe and 1.87 ~ 2.00 Å for N–Fe (C–Fe) bonds, respectively, and the binding energies are $-5.01 \sim -12.03$ eV (Table 1). The Fe₂ dimer exhibits different buckling height in the out-of-plane direction (0.01 ~ 2.06 Å), and meanwhile induces some local vertical distortions on the carbon basal plane (0.09 ~ 0.35 Å). The dimer-substrate coupling strength depends on the size of the hole as well as the saturation degree of the edge atoms. For instance, binding strength between Fe₂ and 4N-V₂, 5N-V₃, and 6N-V₄(a) increases with both N content and hole size. The bonding interaction between Fe₂ and g-C₃N₄ or C₂N is relatively weak, due to the electronic saturation of these two semiconducting carbon nitride monolayers (as

manifested by their large band gaps). In sharp contrast, Fe₂ is strongly anchored on the nitrogen-free V₆ defect that has six unsaturated carbon atoms on the hole edge, thereby leading to the largest binding energy of -12.03 eV.

All the supported Fe₂ dimers are able to chemisorb two CO₂ molecules with total adsorption energies of -0.23 ~ -1.62 eV (compared to -0.11 ~ -1.58 eV for adsorption of single CO₂ molecule), as revealed by Figure 3b. Both CO₂ molecules are bended with O-C-O angle of 141.00 ~ 152.13° and elongated C-O bond lengths of 1.17 ~ 1.29 Å. The C atom in each CO₂ is bonded to the underlying Fe atom with Fe-C bond length of 1.93 ~ 2.12 Å. Furthermore, we investigated the interaction between the dispersed Fe₂ dimers and the CO molecule, which is an important reaction intermediate in the CO₂ reduction process. Our calculations indicate strong binding of CO on the anchored Fe₂ dimers, with adsorption energies of -2.94 ~ -4.04 eV (-1.94 ~ -2.70 eV) for two (one) CO molecules. Consequently, desorption of CO from dual metal centers would be rather difficult, which allows further protonation of CO and thus provides the opportunity for successive C-C coupling.

The distinct binding capability of various supported Fe₂ dimers with gas molecules can be related to the electronic coupling between Fe₂ and the carbon substrate. As displayed in Figure 2c, the amount of charge transfer from Fe₂ to the substrate varies from 0.71 *e* to 0.97 *e*. Generally speaking, less electron transfer leads to higher activity of the Fe₂ dimer for CO₂ and CO chemisorption, which is consistent with the trend of binding energies between Fe₂ and the carbon templates discussed before (Table 1). It is the N content, the degree of electronic saturation of the hole edge, and the bond configuration of Fe₂ in the hole, that jointly determine the coupling strength between the metal dimer and the carbon sheets. Therefore, the nitrogenated 2D holey carbon materials with diverse morphologies and controllable N contents can not only stabilize and disperse metal dimers, but also dictate the electronic structures and activity of the anchored metal dimers. This opens up a universal avenue for modulating the product selectivity for CO₂ reduction, as will be discussed in the following contents.

Note that graphitic N species are inevitably present in the experimentally

synthesized N-doped carbon materials (Lin et al., 2014). To clarify their effect on the activity of the dispersed Fe₂ dimer, we investigated the CO₂ adsorption on Fe₂@6N-V₆ containing various numbers of graphitic N atoms at different distances from the 6N-V₆ hole (Figure S4). For all the considered systems, the CO₂ adsorption energies on the catalysts with and without substitutional N atoms on the graphene lattice differ by less than 0.16 eV, suggesting that existence of the graphitic N species has only minor impact on the catalytic properties of the Fe₂ dimer supported on pyridine holes of 2D carbon substrates.

Figure 4 shows the most efficient pathways for CO₂ reduction toward possible C₁ and C₂ products on the Fe₂ dimer immobilized on various nitrogenated carbon sheets, and the corresponding free energy diagrams of various model systems calculated by the computational hydrogen electrode (CHE) model (Peterson et al., 2010) are given by Figure 5, Figure S5 and Figure S6. We used point (.) to represent the co-adsorption of two carbon intermediates on the catalyst and strigula (–) to indicate the coupling between two carbon intermediates. The maximum Gibbs free energy of formation ΔG among all the reaction steps defines the rate-determine step (RDS) and is thus denoted as ΔG_{RDS} . Overall speaking, formation of C₂ products first requires the activation of dual CO₂ molecules on the catalyst. By going through the carboxyl (COOH*) pathway, two CO* intermediates can be generated. Then, protonation of CO* leads to C₁ products like methanol (CH₃OH) and CH₄. Alternatively, it paves a way to the coupling between two neighboring carbon intermediates, which is energetically favorable and kinetically easy, and finally yields C₂ products (C₂H₅OH and C₂H₄).

Specifically, formation of two CO* species on most of the considered Fe₂ dimers is uphill in the free energy profile, involving energy steps of 0.24 ~ 0.87 eV. Then, reduction of CO* gives rise to HCO* species, which is lower in energy by up to 1.13 eV than the other possible intermediates such as COH* (Figure S7). The CO* → HCO* conversion is endothermic with $\Delta G = 0.49 \sim 1.01$ eV. Further protonation of HCO* leads to HCOH*, and then produces a CH* species by release of a H₂O molecule. The C–C coupling reaction is most likely to occur between a CH* (or CH₂*) species and

the neighboring CO*. Our nudged elastic band (NEB) calculations suggest that the CO-CH* coupling is exothermic and barrierless on all the considered Fe₂ dimers, except for Fe₂@C₂N and Fe₂@C₃N₄ that involve a small kinetic barrier of about 0.22 eV (Table S1). According to previous theoretical studies (Goodpaster et al., 2016; Jiang et al., 2018), Cu(211) and (100) as the typical active surfaces for CO₂ reduction, favor dimerization of CO* or CO-HCO* coupling involving $\Delta G = -0.17 \sim 0.48$ eV. For the present Fe₂ dimers on nitrogenated carbon sheets, however, CO-CO* or CO-HCO* coupling has higher ΔG than the values of CO-CH* by 0.84 \sim 2.42 eV, and thus is unlikely to occur.

Following the C-C coupling, successive reduction of CO-CH* leads to CO-CH₂*, HCO-CH₂*, HCOH-CH₂*, HCOH-CH₃*, and finally yields C₂H₅OH. Alternatively, reduction of HCOH-CH₂* can give rise to CH-CH₂* with release of a H₂O molecule, and further protonation of CH-CH₂* eventually produces C₂H₄. These elementary reactions involve relatively small steps of 0.15 \sim 0.73 eV in free energy profile, and thus would take place readily from the thermodynamic point of view. At the last step, desorption of C₂H₅OH* and CH₂CH₂* is endothermic by 0.11 \sim 0.59 eV and 0.23 \sim 1.76 eV, respectively. For most of the considered Fe₂ dimers, the rate-determine step for C₂H₅OH production is the CO* \rightarrow HCO* conversion, while release of C₂H₄ mainly suffers from the strong binding of CH₂CH₂* on the catalyst.

On the other hand, formation of C₁ products is also possible on the dispersed Fe₂ dimers. As discussed above, HCOH* can be reduced to CH*, followed by the CO-CH* coupling. Alternatively, HCOH* may be protonated to H₂COH*. Then, reduction of H₂COH* yields CH₃OH, or produces CH₂* with release of a H₂O molecule followed by the generation of CH₃* and CH₄. For Fe₂@4N-V₂, Fe₂@6N-V₆ and Fe₂@g-C₃N₄, the CO* \rightarrow HCO* conversion is the rate-determine step for both C₁ products. For Fe₂@6N-V₄(b) and Fe₂@5N-V₃, formation of CH₃OH from H₂COH* protonation requires $\Delta G_{\text{RDS}} = 1.45$ and 0.98 eV, respectively. In particular, Fe₂@C₂N encounters $\Delta G_{\text{RDS}} = 0.94$ eV and a kinetic barrier of 0.77 eV during the reaction of HCOH* \rightarrow H₂COH* for both C₁ products, whereas the competing step of CO-HCOH* \rightarrow

CO-CH* + H₂O has much reduced $\Delta G = -0.30$ eV and a lower kinetic barrier of 0.42 eV (Figure 5a, c). This would lead to high selectivity for C₂ products on Fe₂@C₂N.

Figure 6(a) plots ΔG_{RDS} values for various C₁ and C₂ products from CO₂ reduction on the anchored Fe₂ dimers. Among the four products, C₂H₅OH exhibits the lowest $\Delta G_{\text{RDS}} = 0.57 \sim 1.01$ eV, and the highest activity is achieved by Fe₂@6N-V₆ owing to its moderate adsorption strength with the reaction intermediates (indicated by the dashed blue line in Figure 6a). Formation of C₂H₄ is less favorable with $\Delta G_{\text{RDS}} = 0.58 \sim 1.76$ eV due to the strong binding of CH₂CH₂* on the Fe₂ dimers. Fe₂@6N-V₄(a), Fe₂@4N-V₂, Fe₂@6N-V₆ and Fe₂@g-C₃N₄ exhibit similar selectivity for C₂H₅OH, CH₃OH, and CH₄, while Fe₂@5N-V₃ favors both C₂H₅OH and CH₄ products. Remarkable selectivity for C₂H₅OH is obtained for Fe₂@C₂N and Fe₂@6N-V₄(b) with $\Delta G_{\text{RDS}} = 0.70$ and 0.59 eV, respectively, notably lower than ΔG_{RDS} values for the other products (above 0.94 and 0.85 eV, respectively). Hence, these supported Fe₂ dimers have competitive activity but distinct selectivity with regard to the conventional Cu based catalysts. It is known that Cu crystals mainly produce CO under low electrode potentials, while CH₄ and C₂H₄ are the main products at sufficiently high electrode potentials (about -1.0 V vs. RHE in experiment) (Dai et al., 2017; Mistry et al., 2016). Previous calculations revealed that Cu(211) surface encounters $\Delta G_{\text{RDS}} = 0.74$ eV for CH₄ and C₂H₄, while formation of CO is much more favorable with $\Delta G_{\text{RDS}} = 0.41$ eV due to the relatively weak adsorption of CO on the Cu surface (adsorption energy $\Delta E = -1.01$ eV) (Peterson et al., 2010). Differently, release of CO is prohibited on the present Fe₂ dimers that have strong adsorption energy of $\Delta E = -2.94 \sim -4.04$ eV with CO molecule.

The unique geometry and favorable adsorption properties of the Fe₂ dimers immobilized on carbon substrates bring about inimitable advantages for their catalytic behavior. First, CO as an inevitable and even dominant product of CO₂ reduction on many metal catalysts, severely limits the formation of higher-energy-density products (Zhu et al., 2014; Sarfraz et al., 2016; Peng et al., 2018); but it would be largely suppressed on the anchored Fe₂ dimers. Second, the adjacent dual metal centers and

their strong binding with CO pave an efficient pathway for C–C coupling reaction; in contrast, C–C coupling only occurs on metal surfaces with homogeneously distributed reaction sites when the coverage of CO is sufficiently high (Morales-Guio et al., 2018; Huang et al., 2017). Third, the difficult desorption of C₂H₄ from the Fe₂ dimers may result in superior selectivity for C₂H₅OH, which is a clean liquid fuel with high heating value. For most of the Cu based catalysts, however, the yield of C₂H₅OH is quite low compared to C₂H₄ (Liang et al., 2018).

At last, we assess the activity of these supported Fe₂ dimers for HER, which is a competing reaction against CO₂ reduction and highly affects the efficiency of CO₂ conversion (Zhu et al., 2016; Cui et al., 2017). Figure 6(b) plots the competition between adsorption of H* species and CO₂ molecule on the Fe₂ dimers. The H* adsorption energy ranges from –1.52 eV to –0.28 eV. For Fe₂@5N-V₃, Fe₂@6N-V₆, Fe₂@C₂N and Fe₂@C₃N₄, the adsorption strength of H* species is notably weaker than that of CO₂ molecule by 0.09 ~ 0.67 eV, implying that CO₂ reduction would prevail over HER on these catalysts with either high activity or superior selectivity. For Fe₂@4N-V₂, Fe₂@6N-V₄(a) and Fe₂@6N-V₄(b), the H* adsorption strength is stronger than that of CO₂, which may suppress the CO₂ reduction. In short, our results confirm that the Fe₂ dimers immobilized on various nitrogenated carbon materials universally possess outstanding activity for C₂H₅OH synthesis from CO₂ reduction, and desired selectivity can be further achieved by selecting proper carbon substrates.

CONCLUSION

In summary, we exploited dispersed 3*d* transition metal dimers for CO₂ reduction to selectively produce liquid fuels. Comprehensive first-principles calculations show that nitrogenated holey carbon materials not only serve as templates to stabilize small metal clusters, but also dictate their electronic structures. Specifically, controlling the metal-substrate coupling strength allows effective modulation of both activity and product selectivity. As a consequence, the spatially confined dual reaction centers within the carbon matrix exhibit the following advantageous catalytic behavior: (1)

simultaneous fixation of two CO₂ molecules, (2) prohibition of CO desorption, (3) exclusive pathway for C–C coupling, (4) high activity for C₂H₅OH production irrelevant to the type of substrate. A number of immobilized dimer systems with outstanding activity and selectivity have been obtained. In particular, a Fe₂ dimer embedded in the C₂N monolayer exhibits remarkable selectivity for C₂H₅OH against the other C₁ and C₂ products as well as HER. These theoretical findings provide vital guidance for atomically precise design of the dispersed metal clusters for converting the greenhouse gas to high-energy fuels and high-value chemicals.

Limitations of the Study

This study systematically exploited 3*d* transition metal dimers anchored on nitrogenated holey carbon monolayers for selective reduction of CO₂ to liquid fuels, and screened suitable metal elements and carbon templates with high selectivity for ethanol. However, experimental realization of such superior subnano catalysts relies on the preparation of metal clusters with specific size supported on some given substrates, which may be challenging and requires the development of advanced synthesis methods.

METHODS

All methods can be found in the accompanying Transparent Methods supplemental file.

Acknowledgements

This work was financially supported by the National Natural Science Foundation of China (11974068, 91961204). The authors acknowledge the computer resources provided by the Supercomputing Center of Dalian University of Technology.

Author Contributions

S. Zhou conceived the idea; Y. Zhao carried out the calculation; S. Zhou and J. Zhao supervise the research. All authors wrote the paper.

Declaration of Interests

The authors declare no competing interests.

REFERENCES

Birdja, Y. Y.; Pérez-Gallent, E., Figueiredo, M. C., Göttle, A. J., Calle-Vallejo, F., Koper, M. T. M. (2019). Advances and Challenges in Understanding the Electrocatalytic Conversion of Carbon Dioxide to Fuels. *Nat. Energy* 4, 732-745.

Jia, C., Dastafkan, K., Ren, W., Yang, W., Zhao, C. (2019). Carbon-Based Catalysts for Electrochemical CO₂ Reduction. *Sustain. Energy Fuels* 3, 2890-2906.

Amal, R., Zhao, H., Wang, D., Wang, L. (2017). Renewable Energy Conversion and Storage. *Adv. Energy Mater.* 7, 1703091.

Zheng, Y., Vasileff, A., Zhou, X., Jiao, Y., Jaroniec, M., Qiao, S. Z. (2019). Understanding the Roadmap for Electrochemical Reduction of CO₂ to Multi-Carbon Oxygenates and Hydrocarbons on Copper-Based Catalysts. *J. Am. Chem. Soc.* 141, 7646-7659.

Kim, D., Kley, C. S., Li, Y., Yang, P. (2017). Copper Nanoparticle Ensembles for Selective Electroreduction of CO₂ to C₂-C₃ Products. *Proc. Natl. Acad. Sci. U.S.A.* 114, 10560-10565.

Zhou, Y., Che, F., Liu, M., Zou, C., Liang, Z., De Luna, P., Yuan, H., Li, J., Wang, Z., Xie, H., et al. (2018). Dopant-Induced Electron Localization Drives CO₂ Reduction to C₂ Hydrocarbons. *Nat. Chem* 10, 974-980.

Gao, D., Arán-Ais, R. M., Jeon, H. S., Roldan Cuenya, B. (2019). Rational Catalyst and Electrolyte Design for CO₂ Electroreduction Towards Multicarbon Products. *Nat. Catal.* 2, 198-210.

Wang, Y., Han, P., Lv, X., Zhang, L., Zheng, G. (2018). Defect and Interface Engineering for Aqueous Electrocatalytic CO₂ Reduction. *Joule* 2, 2551-2582.

Wang, L., Chen, W., Zhang, D., Du, Y., Amal, R., Qiao, S., Wu, J., Yin, Z. (2019). Surface Strategies for Catalytic CO₂ Reduction: from Two-Dimensional Materials to Nanoclusters to Single Atoms. *Chem. Soc. Rev.* 48, 5310-5349.

Bayatsarmadi, B., Zheng, Y., Vasileff, A., Qiao, S. Z. (2017). Recent Advances in Atomic Metal Doping of Carbon-Based Nanomaterials for Energy Conversion. *Small* 13, 1700191.

Chen, Y. N., Zhang, X., Zhou, Z. (2019). Carbon-Based Substrates for Highly Dispersed Nanoparticle and Even Single-Atom Electrocatalysts. *Small Methods* 3, 1900050.

Cheng, Y., Zhao, S., Johannessen, B., Veder, J. P., Saunders, M., Rowles, M. R., Cheng, M., Liu, C., Chisholm, M. F., De Marco, R., et al. (2018). Atomically Dispersed Transition Metals on Carbon Nanotubes with Ultrahigh Loading for Selective Electrochemical Carbon Dioxide Reduction. *Adv. Mater.* 30, e1706287.

Jiang, K., Siahrostami, S., Zheng, T., Hu, Y., Hwang, S., Stavitski, E., Peng, Y., Dynes, J., Gangisetty, M., Su, D., et al. (2018). Isolated Ni Single Atoms in Graphene Nanosheets for High-Performance CO₂ Reduction. *Energy & Environ. Sci.* 11, 893-903.

Zhang, C., Yang, S., Wu, J., Liu, M., Yazdi, S., Ren, M., Sha, J., Zhong, J., Nie, K., Jalilov, A. S., et al. (2018). Electrochemical CO₂ Reduction with Atomic Iron-Dispersed on Nitrogen-Doped Graphene. *Adv. Energy Mater.* 8, 1703487.

Yang, H. B., Hung, S.-F., Liu, S., Yuan, K., Miao, S., Zhang, L., Huang, X., Wang, H.-Y., Cai, W., Chen, R., et al. (2018). Atomically Dispersed Ni(I) as the Active Site for Electrochemical CO₂ Reduction. *Nat. Energy* 3, 140-147.

Wang, T., Zhao, Q., Fu, Y., Lei, C., Yang, B., Li, Z., Lei, L., Wu, G., Hou, Y. (2019). Carbon-Rich Nonprecious Metal Single Atom Electrocatalysts for CO₂ Reduction and Hydrogen Evolution. *Small Methods*, 1900210.

Ren, W., Zhao, C. (2019). Paths Towards Enhanced Electrochemical CO₂ Reduction. *Natl. Sci. Rev.* nwz121.

Ju, W., Bagger, A., Hao, G. P., Varela, A. S., Sinev, I., Bon, V., Roldan Cuenya, B., Kaskel, S., Rossmeisl, J., Strasser, P. (2017). Understanding Activity and Selectivity of Metal-Nitrogen-Doped Carbon Catalysts for Electrochemical Reduction of CO₂. *Nat. Commun.* 8, 944.

Bagger, A., Ju, W., Varela, A. S., Strasser, P., Rossmeisl, J. (2017). Single Site Porphyrine-Like Structures Advantages Over Metals for Selective Electrochemical CO₂ Reduction. *Catal. Today* 288, 74-78.

Ye, W., Chen, S., Lin, Y., Yang, L., Chen, S., Zheng, X., Qi, Z., Wang, C., Long, R., Chen, M., et al. (2019). Precisely Tuning the Number of Fe Atoms in Clusters on N-Doped Carbon toward Acidic Oxygen Reduction Reaction. *Chem* 5, 2865-2878.

Wang, J., Huang, Z., Liu, W., Chang, C., Tang, H., Li, Z., Chen, W., Jia, C., Yao, T., Wei, S., et al. (2017). Design of N-Coordinated Dual-Metal Sites: A Stable and Active Pt-Free Catalyst for Acidic Oxygen Reduction Reaction. *J. Am. Chem. Soc.* 139, 17281-17284.

Wang, J., Gan, L. Y., Zhang, W. Y., Peng, Y. C., Yu, H., Yan, Q. Y., Xia, X. H., Wang, X. (2018). In Situ Formation of Molecular Ni-Fe Active Sites on Heteroatom-Doped Graphene as a Heterogeneous Electrocatalyst Toward Oxygen Evolution. *Sci. Adv.* 4, eaap7970.

Zhou, P., Hou, X., Chao, Y., Yang, W., Zhang, W., Mu, Z., Lai, J., Lv, F., Yang, K., Liu, Y., et al. (2019). Synergetic Interaction Between Neighboring Platinum and Ruthenium Monomers Boosts CO Oxidation. *Chem. Sci.* 10, 5898-5905.

Ren, W., Tan, X., Yang, W., Jia, C., Xu, S., Wang, K., Smith, S. C., Zhao, C. (2019). Isolated Diatomic Ni-Fe Metal-Nitrogen Sites for Synergistic Electroreduction of CO₂. *Angew. Chem. Int. Ed.* 58, 6972-6976.

Zhao, J., Zhao, J., Li, F., Chen, Z. (2018). Copper Dimer Supported on a C₂N Layer as an Efficient Electrocatalyst for CO₂ Reduction Reaction: A Computational Study. *J. Phys. Chem. C* 122, 19712-19721.

Li, Y., Su, H., Chan, S. H., Sun, Q. (2015). CO₂ Electroreduction Performance of Transition Metal Dimers Supported on Graphene: A Theoretical Study. *ACS Catal.* 5, 6658-6664.

He, H., Morrissey, C., Curtiss, L. A., Zapol, P. (2018). Graphene-Supported Monometallic and Bimetallic Dimers for Electrochemical CO₂ Reduction. *J. Phys. Chem. C* 122, 28629-28636.

Shen, H., Li, Y., Sun, Q. (2017). CO₂ Electroreduction Performance of Phthalocyanine Sheet with Mn Dimer: A Theoretical Study. *J. Phys. Chem. C* 121, 3963-3969.

Xue, Y., Wu, B., Jiang, L., Guo, Y., Huang, L., Chen, J., Tan, J., Geng, D., Luo, B., Hu, W., et al. (2012). Low Temperature Growth of Highly Nitrogen-Doped Single Crystal Graphene Arrays by Chemical Vapor Deposition. *J. Am. Chem. Soc.* 134, 11060-110603.

Xu, H., Ma, L., Jin, Z. Nitrogen-doped graphene: Synthesis, (2018). Characterizations and Energy Applications. *J. Energy Chem.* 27, 146-160.

Qu, L., Liu, Y., Baek, J. B., Dai, L. (2010). Nitrogen-Doped Graphene as Efficient Metal-Free Electrocatalyst for Oxygen Reduction in Fuel Cells. *ACS Nano* 4, 1321-1326.

Sheng, Z. H., Shao, L., Chen, J. J., Bao, W. J., Wang, F. B., Xia, X. H. (2011). Catalyst-Free Synthesis of Nitrogen-Doped Graphene Via Thermal Annealing Graphite Oxide with Melamine and Its Excellent Electrocatalysis. *ACS Nano* 5, 4350-4358.

Sarau, G., Heilmann, M., Bashouti, M., Latzel, M., Tessarek, C., Christiansen, S. (2017). Efficient Nitrogen Doping of Single-Layer Graphene Accompanied by Negligible Defect Generation for Integration into Hybrid Semiconductor Heterostructures. *ACS Appl. Mater. Interfaces* 9, 10003-10011.

Lin, Y. C., Teng, P. Y., Yeh, C. H., Koshino, M., Chiu, P. W., Suenaga, K. (2015). Structural and Chemical Dynamics of Pyridinic-Nitrogen Defects in Graphene. *Nano Lett.* 15, 7408-7413.

He, Z., He, K., Robertson, A. W., Kirkland, A. I., Kim, D., Ihm, J., Yoon, E., Lee, G. D., Warner,

J. H. (2014). Atomic Structure and Dynamics of Metal Dopant Pairs in Graphene. *Nano Lett.* 14, 3766-3772.

Wang, Q., Ji, Y., Lei, Y., Wang, Y., Wang, Y., Li, Y., Wang, S. (2018). Pyridinic-N-Dominated Doped Defective Graphene as a Superior Oxygen Electrocatalyst for Ultrahigh-Energy-Density Zn–Air Batteries. *ACS Energy Lett.* 3, 1183-1191.

Robertson, A. W., Lee, G. D., He, K., Gong, C., Chen, Q., Yoon, E., Kirkland, A. I., Warner, J. H. (2015). Atomic Structure of Graphene Subnanometer Pores. *ACS Nano* 9, 11599-11607.

Luo, G., Liu, L., Zhang, J., Li, G., Wang, B., Zhao, J. (2013). Hole Defects and Nitrogen Doping in Graphene: Implication for Supercapacitor Applications. *ACS Appl. Mater. Interfaces* 5, 11184-11193.

Zhao, H., Yu, H., Quan, X., Chen, S., Zhang, Y., Zhao, H., Wang, H. (2014). Fabrication of Atomic Single Layer Graphitic-C₃N₄ and Its High Performance of Photocatalytic Disinfection Under Visible Light Irradiation. *Appl. Catal. B-Environ.* 152, 46-50.

Mahmood, J., Lee, E. K., Jung, M., Shin, D., Jeon, I. Y., Jung, S. M., Choi, H. J., Seo, J. M., Bae, S. Y., Sohn, S. D., et al. (2015). Nitrogenated Holey Two-Dimensional Structures. *Nat. Commun.* 6, 6486.

Tian, S., Fu, Q., Chen, W., Feng, Q., Chen, Z., Zhang, J., Cheong, W. C., Yu, R., Gu, L., Dong, J., et al. (2018). Carbon Nitride Supported Fe₂ Cluster Catalysts with Superior Performance for Alkene Epoxidation. *Nat. Commun.* 9, 2353.

Hammer, B., Nørskov, J. K. (2000). Theoretical Surface Science and Catalysis—Calculations and Concepts. *Adv. Catal.* 45, 71-129.

Lin, Y.-P., Ksari, Y., Prakash, J., Giovanelli, L., Valmalette, J.-C., Themlin, J.-M. (2014). Nitrogen-Doping Processes of Graphene by a Versatile Plasma-Based Method. *Carbon* 73, 216-224.

Peterson, A. A., Abild-Pedersen, F., Studt, F., Rossmeisl, J., Nørskov, J. K. (2010). How Copper Catalyzes the Electroreduction of Carbon Dioxide into Hydrocarbon Fuels. *Energy Environ. Sci.* 3, 1311-1315.

Goodpaster, J. D., Bell, A. T., Head-Gordon, M. (2016). Identification of Possible Pathways for C–C Bond Formation during Electrochemical Reduction of CO₂: New Theoretical Insights from an Improved Electrochemical Model. *J. Phys. Chem. Lett.* 7, 1471-1477.

Jiang, K., Sandberg, R. B., Akey, A. J., Liu, X., Bell, D. C., Nørskov, J. K., Chan, K., Wang, H. (2018). Metal Ion Cycling of Cu Foil for Selective C–C Coupling in Electrochemical CO₂ Reduction. *Nat. Catal.* 1, 111-119.

Dai, L., Qin, Q., Wang, P., Zhao, X. J., Hu, C. Y., Liu, P. X., Qin, R. X., Chen, M., Ou, D. H., Xu, C. F., et al. (2017). Ultrastable Atomic Copper Nanosheets for Selective Electrochemical Reduction of Carbon Dioxide. *Sci. Adv.* 3, e1701069.

Mistry, H., Varela, A. S., Bonifacio, C. S., Zegkinoglou, I., Sinev, I., Choi, Y.-W., Kisslinger, K., Stach, E. A., Yang, J. C., Strasser, P., et al. (2016). Highly Selective Plasma-Activated Copper Catalysts for Carbon Dioxide Reduction to Ethylene. *Nat. Commun.* 7, 12123.

Zhu, W., Zhang, Y. J., Zhang, H., Lv, H., Li, Q., Michalsky, R., Peterson, A. A., Sun, S. (2014). Active and Selective Conversion of CO₂ to CO on Ultrathin Au Nanowires. *J. Am. Chem. Soc.* 136, 16132-16135.

Sarfraz, S., Garcia-Esparza, A. T., Jedidi, A., Cavallo, L., Takanabe, K. (2016). Cu–Sn Bimetallic Catalyst for Selective Aqueous Electroreduction of CO₂ to CO. *ACS Catal.* 6, 2842-2851.

Peng, X., Karakalos, S. G., Mustain, W. E. (2018). Preferentially Oriented Ag Nanocrystals with Extremely High Activity and Faradaic Efficiency for CO₂ Electrochemical Reduction to CO. *ACS Appl. Mater. Interfaces* 10, 1734-1742.

Morales-Guio, C. G., Cave, E. R., Nitopi, S. A., Feaster, J. T., Wang, L., Kuhl, K. P., Jackson, A., Johnson, N. C., Abram, D. N., Hatsukade, T., et al. (2018). Improved CO₂ Reduction Activity Towards C₂₊ Alcohols on a Tandem Gold on Copper Electrocatalyst. *Nat. Catal.* 1, 764-771.

Huang, Y., Handoko, A. D., Hirunsit, P., Yeo, B. S. (2017). Electrochemical Reduction of CO₂ Using Copper Single-Crystal Surfaces: Effects of CO* Coverage on the Selective Formation of Ethylene. *ACS Catal.* 7, 1749-1756.

Liang, Z. Q., Zhuang, T. T., Seifitokaldani, A., Li, J., Huang, C. W., Tan, C. S., Li, Y., De Luna, P., Dinh, C. T., Hu, Y., et al. (2018). Copper-on-Nitride Enhances the Stable Electrosynthesis of Multi-Carbon Products from CO₂. *Nat. Commun.* 9, 3828.

Zhu, D. D., Liu, J. L., Qiao, S. Z. (2016). Recent Advances in Inorganic Heterogeneous Electrocatalysts for Reduction of Carbon Dioxide. *Adv. Mater.* 28, 3423-3452.

Cui, X., Pan, Z., Zhang, L., Peng, H., Zheng, G. (2017). Selective Etching of Nitrogen-Doped Carbon by Steam for Enhanced Electrochemical CO₂ Reduction. *Adv. Energy Mater.* 7, 1701456.

Table 1. Formation energy (E_{form}) of various nitrogenated 2D holey carbon materials, binding energy (E_b) of a Fe_2 dimer on the carbon sheet, bond length (d) of Fe–Fe and N–Fe/C–Fe bonds, Mulliken charge transfer (CT) from Fe_2 to the carbon sheet, adsorption energy of a CO_2 molecule ($\Delta E_{\text{CO}_2^*}$) on the supported Fe_2 dimer.

Substrate	E_{form} (eV/Å)	E_b (eV)	d (Å)		CT (e)	$\Delta E_{\text{CO}_2^*}$ (eV)
			Fe–Fe	N–Fe		
4N-V ₂	0.17	−5.01	2.09	1.98	0.71	−1.02
5N-V ₃	0.19	−7.33	1.91	1.87	0.97	−1.15
6N-V ₄ (a)	0.20	−9.47	2.21	1.94	0.96	−0.11
6N-V ₄ (b)	0.21	−7.48	2.14	1.98	0.81	−1.15
6N-V ₆	0.16	−6.02	1.96	2.00	0.76	−1.12
C ₂ N	--	−5.80	2.01	1.97	0.74	−0.64
g-C ₃ N ₄	--	−5.09	1.98	1.99	0.72	−1.58
V ₆	0.67	−12.03	2.21	1.94	0.87	−0.30

Table 2. Binding energy (E_b) of various 3d transition metal dimers anchored on the 6N- V_6 monolayer, bond lengths (d) of metal dimer (M–M) and N–metal (N–M), adsorption energy of single and dual CO_2 molecules on the supported metal dimers (ΔE), and the d band center (ε_d) of the supported metal dimers (Hammer et al., 2000).

Metal dimer	E_b (eV)	d (Å)		ΔE (eV)		ε_d (eV)
		M–M	N–M	CO_2	$2CO_2$	
Sc ₂	–10.28	2.79	2.09	–3.40	–3.71	1.16
Ti ₂	–8.50	2.17	1.99	–2.85	–3.31	0.62
V ₂	–8.80	2.14	1.96	–2.26	--	0.41
Cr ₂	–4.99	2.16	1.97	–1.44	–0.76	0.07
Mn ₂	–6.52	2.04	2.01	–1.05	–0.48	–0.42
Fe ₂	–6.02	1.96	2.00	–1.12	–0.50	–1.00
Co ₂	–5.71	2.10	1.95	–1.20	--	–1.09
Ni ₂	–5.93	2.17	2.00	–0.82	--	–1.12
Cu ₂	–4.29	2.35	1.96	–0.35	--	–2.08

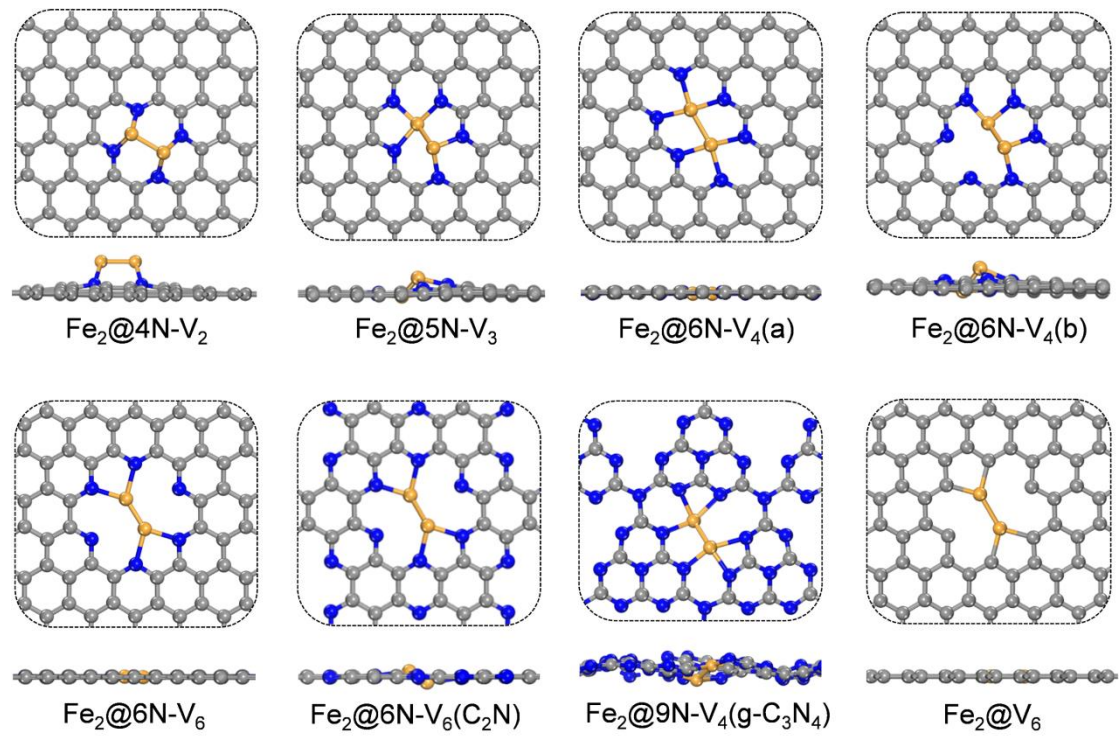


Figure 1. Atomic structures of a Fe_2 dimer anchored on various nitrogenated holey carbon monolayers (top panel: top view; bottom panel: side view). The C, N and Fe atoms are shown in grey, blue and orange colors, respectively.

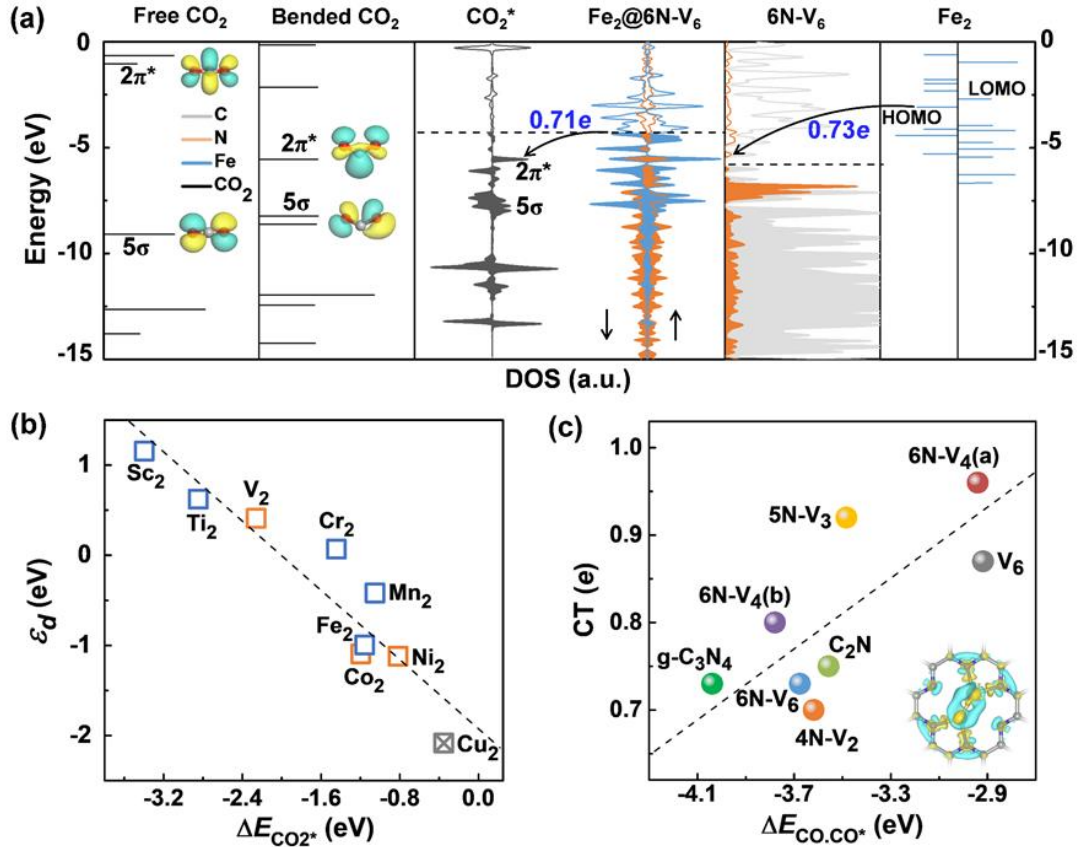


Figure 2. (a) From left to right: molecular orbital levels or local density of states (DOS) of a free and a bended (with C–O–C angle of 130°) CO₂ molecule in vacuum, an adsorbed CO₂ molecule on Fe₂@6N-V₆, an individual 6N-V₆ monolayer and a Fe₂ dimer. The insets display the HOMO and LUMO charge densities of CO₂. The energy is relative to the vacuum. The dashed line shows the Fermi level, with the occupied states shadowed. (b) The *d* band center (ε_d) of various supported 3*d* transition metal dimers as a function of the adsorption energy of single CO₂ molecule. The blue/orange/grey symbols denote that two/one/none CO₂ molecule can be chemisorbed on the metal dimer. The dashed line is a linear fit of the data points. (c) Charge transfer (CT) from the Fe₂ dimer to various nitrogenated carbon holey monolayer as a function of the adsorption energy of dual CO molecules. The dashed line is a linear fit of the data points. The insert shows the differential charge density of Fe₂@6N-V₆. The yellow and cyan colors represent the electron accumulation and depletion regions, respectively, with an isosurface value of 0.005 e/Å³.

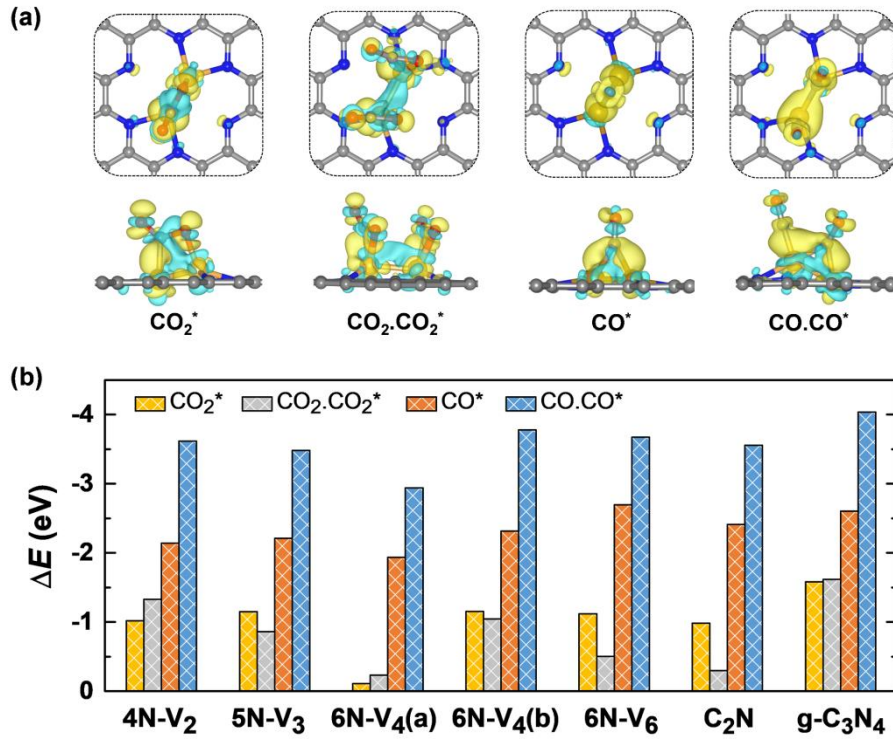


Figure 3. (a) From left to right: differential charge densities of single and dual CO₂ molecules, single and dual CO molecules adsorbed on Fe₂@6N-V₆. The yellow and cyan colors represent the electron accumulation and depletion regions, respectively, with an isosurface value of $0.005 e/\text{\AA}^3$. (b) Adsorption energies of single and dual CO₂ and CO molecules on the Fe₂ dimer anchored on various nitrogenated holey carbon monolayers. The C, N, O and Fe atoms are shown in grey, blue, red and orange colors, respectively.

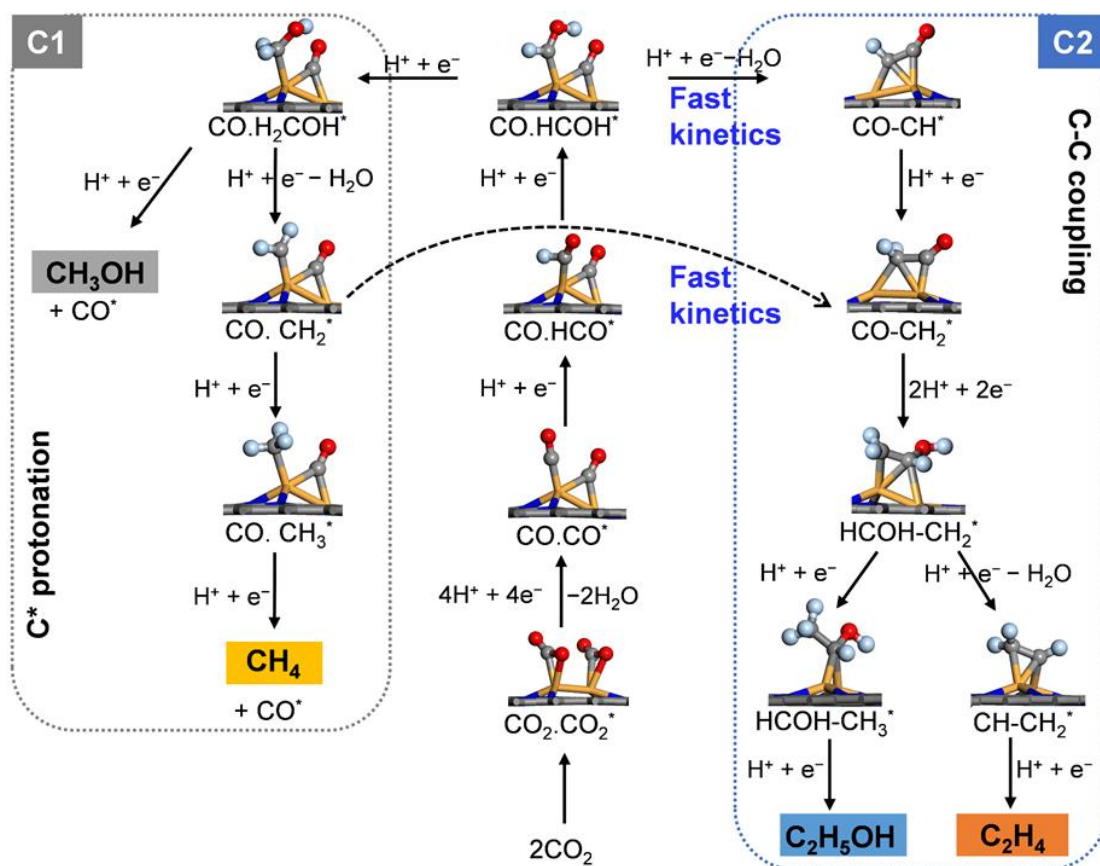


Figure 4. The CO₂ reduction pathways to various C₁ and C₂ products on the supported Fe₂ dimer. The H, C, N, O and Fe atoms are shown in light blue, grey, blue, red and orange colors, respectively.

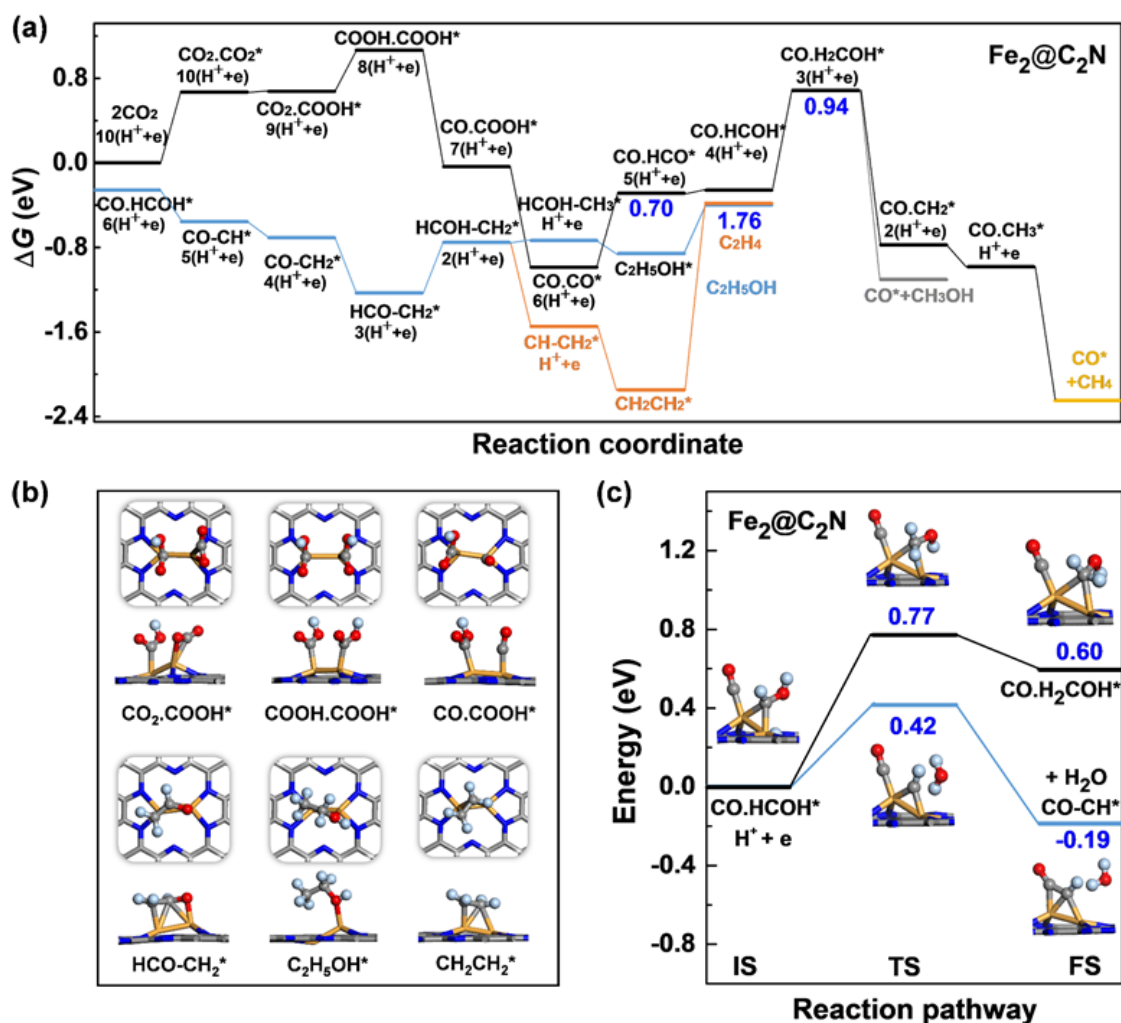


Figure 5. (a) Free energy diagram of CO₂ reduction to various C₁ and C₂ products (indicated by different colors) on Fe₂@C₂N. The blue numbers, from left to right, give the Gibbs free energy of formation for the rate-determine step of C₂H₅OH, C₂H₄ and CH₃OH/CH₄. The local structures of selected reaction intermediates are presented in (b). The H, C, N, O and Fe atoms are shown in light blue, grey, blue, red and orange colors, respectively. (c) Competing reactions of CO.HCOH to form C₁ and C₂ intermediates on Fe₂@C₂N. The insets display the structures of initial state (IS), transition state (TS) and final state (FS). The blue numbers give the kinetic barriers (middle) and heat of reaction (right).

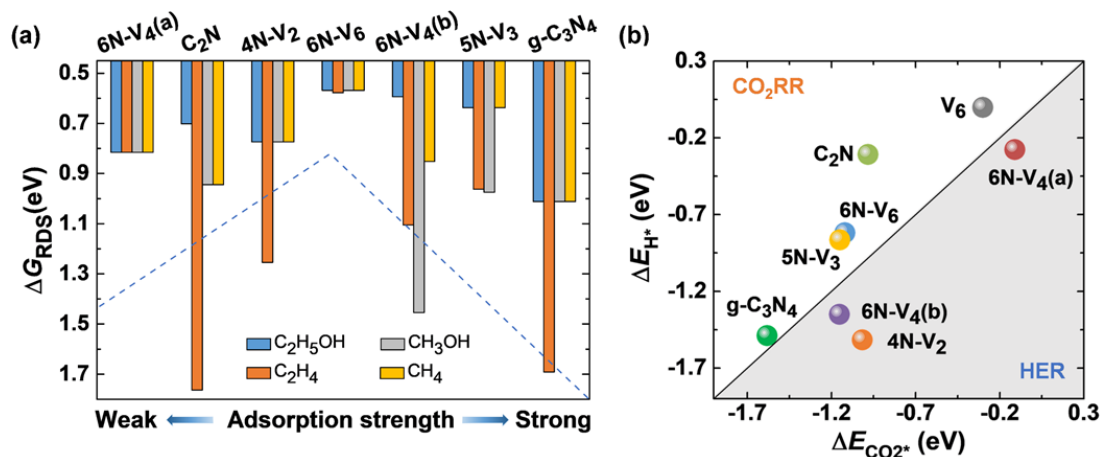


Figure 6. (a) Gibbs free energy of formation for the rate-determine step (ΔG_{RDS}) for various C₁ and C₂ products from CO₂ reduction, and (b) competition between adsorption of a CO₂ molecule and a H* species on the Fe₂ dimer anchored on various nitrogenated holey carbon monolayers.